NANO LETTERS

pubs.acs.org/NanoLett Letter

Dimensional Control of Octahedral Tilt in $SrRuO_3$ via Infinite-Layered Oxides

Shan Lin, Qinghua Zhang, Xiahan Sang, Jiali Zhao, Sheng Cheng, Amanda Huon, Qiao Jin, Shuang Chen, Shengru Chen, Wenjun Cui, Haizhong Guo, Meng He, Chen Ge, Can Wang, Jiaou Wang, Michael R. Fitzsimmons, Lin Gu, Tao Zhu, Kuijuan Jin,* and Er-Jia Guo*

Cite This: https://doi.org/10.1021/acs.nanolett.1c00352 Read Online

ACCESS | Metrics & More | Article Recommendations | Supporting Information

ABSTRACT: Manipulation of octahedral distortion at atomic scale is an effective means to tune the ground states of functional oxides. Previous work demonstrates that strain and film thickness are variable parameters to modify the octahedral parameters. However, selective control of bonding geometry by structural propagation from adjacent layers is rarely studied. Here we propose a new route to tune the ferromagnetism in $SrRuO_3$ (SRO) ultrathin layers by oxygen coordination of adjacent $SrCuO_2$ (SCO) layers. The infinite-layered CuO_2 exhibits a structural transformation from "planar-type" to "chain-type" with reduced film thickness. Two orientations dramatically modify the polyhedral connectivity at the interface, thus altering the octahedral distortion of SRO. The local structural variation changes the spin state of Ru and orbital hybridization strength, leading to a significant change in the magnetoresistance and anomalous Hall resistivity. These findings could launch investigations into adaptive control of functionalities in quantum oxide heterostructures using oxygen coordination.

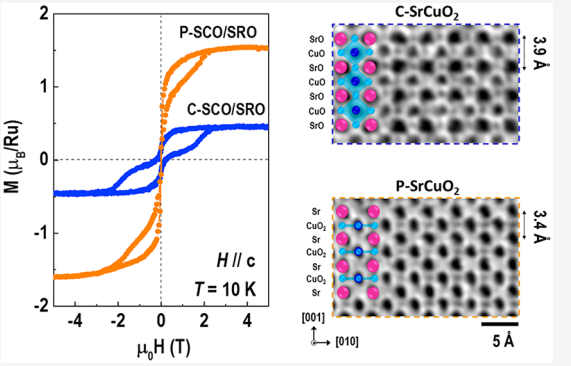

KEYWORDS: *low-dimensional heterostructure, magnetic anisotropy, anomalous Hall conductance, polarized neutron reflectometry*

Engineering octahedral connectivity has been a central research theme in complex oxide heterostructures.[1,2] Atomic modification of octahedral rotation and tilt dramatically changes the bond angle and bond length, resulting in an effective control of directional hybridization of d-electrons and orbital degeneracy. The transport and magnetic properties of correlated perovskite oxides will be modified accordingly due to the intrinsic strong electron−lattice correlations.[3,4] Conventionally, the substrate-induced epitaxial strain effectively changes the octahedral parameters, whose tilting angle and orientation are controlled by the magnitude and sign of the misfit strain.[5−7] The misfit strain relaxes with increasing film thickness. The modification of octahedra normally does not exceed tens of unit cells (u.c.) in a single film, leading to the thickness-dependent electronic and magnetic phase transitions.[8,9]

$SrRuO_3$ (SRO) is a typical ferromagnetic metal with orthorhombic crystalline symmetry in its bulk form.[10−13] It has attracted considerable attention because the structural symmetry and octahedral distortion of SRO thin films are extremely sensitive to the type of strain.[14−16] Another approach to modify the octahedral distortion of SRO is the interfacial engineering of oxygen coordination environment by inserting a buffer layer (such as, $Ca_{0.5}Sr_{0.5}TiO_3$)[17] or capping a top layer (such as, $SrTiO_3$,[18] $LaNiO_3$,[19] etc.) with different crystalline symmetries and octahedral tilt patterns. This leads to the stabilization of a Ru−O−Ru bond angle in the entire SRO layer that is dramatically different from an SRO single layer or bulk SRO. The octahedral distortion thus implicitly controls the magnetic anisotropy and triggers an emergent topological Hall effect.[20−24]

Although various approaches have been applied to modify the octahedral distortion of SRO, control of bonding geometry via the structural propagation from adjacent layers is the rare case.[25−28] Interface effects in the SRO heterostructures with dissimilar crystalline symmetry is scarcely reported, suggesting a great potential in designing artificial heterostructures for harvesting novel functionalities. In this work, we demonstrate the first example of using structural transformation in an infinite layered $SrCuO_2$ (SCO) compound to tune magnetic responses in an adjacent SRO ultrathin layer. The octahedral distortion and lattice tetragonality of SRO layers are controlled

Received: January 26, 2021
Revised: March 12, 2021

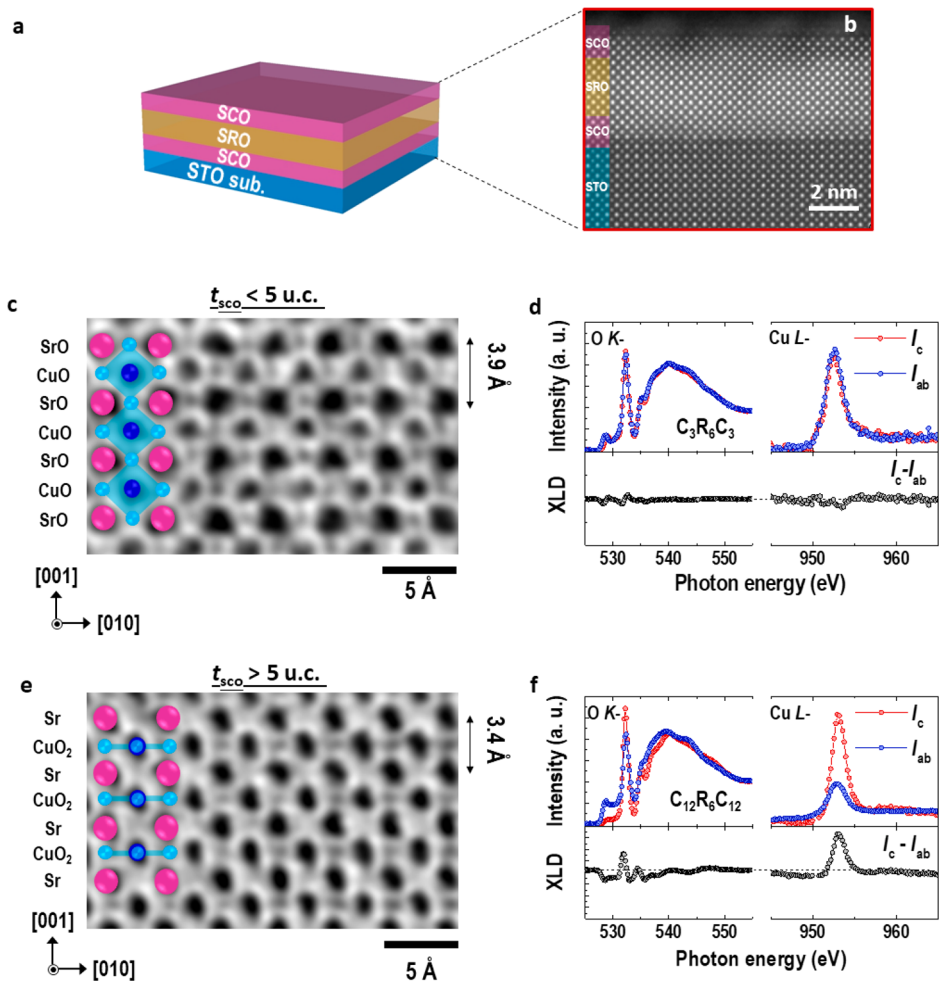

Figure 1. Dimensional control of oxygen coordination and electronic state in $SrCuO_2/SrRuO_3/SrCuO_2$ (SCO/SRO/SCO, $C_nR_mC_n$) trilayers, where n and m represent the number of unit cells of SCO and SRO layers, respectively. (a) Schematic illustration for a $C_nR_mC_n$ trilayer grown on STO substrate. (b) Cross-sectional HAADF-STEM image of a representative $C_3R_6C_3$ trilayer. (c) and (e) Schematic illustrations for the oxygen coordination of $SrCuO_2$ with chain-type (t_{SCO} < 5 u.c.) and planar-type (t_{SCO} > 5 u.c.) structures, respectively. ABF-STEM images shown on the right side are the representative SCO layers in the trilayers. These results indicate the change of oxygen coordination with increasing SCO thickness. All STEM images were taken along the pseudocubic [100] zone axis. (d) and (f) Polarization dependent XAS of O K-edge and Cu L_2-edge for $C_3R_6C_3$ and $C_{12}R_6C_{12}$ trilayers, respectively. The bottom panels in d and f show the X-ray linear dichroism (XLD) calculated from (I_c–I_{ab}), demonstrating a distinct orbital polarization in $C_nR_mC_n$ trilayers with different oxygen coordination.

by the oxygen coordination of SCO, in which the CuO_2 layers transform from a "planar-type" SCO (P-SCO) to "chain-type" SCO (C-SCO) as film thickness is constrained below 5 u.c.[29−32] We observe an enhanced magnetoresistance but reduced anomalous Hall conductance in SRO layers with suppressed octahedral tilt.

Two sets of $[SCO_n/SRO_6/SCO_n]$ ($C_nR_6C_n$) trilayers were deposited on (001)-oriented $SrTiO_3$ substrates by pulsed laser deposition, where n represents the number of u. c. of SCO layers. The SRO layers are sandwiched between two inactive SCO layers to reduce the impact from $SrTiO_3$ substrates, as shown in Figure 1a. SCO is used as inactive layers to tune the structural parameters of SRO. We fix the layer thickness of SRO to be 6 u. c., which is just beyond the critical thickness of metal-to-insulator transition (MIT) (Figure S1). In this phase-instability regime, the magnetic and transport properties of SRO ultrathin layer are extremely sensitive to the structural variations. X-ray diffraction measurements indicate the good crystallinity and as-designed thicknesses of each layer (Figure S2). Figure 1b shows a cross-sectional high-angle annular dark-field (HAADF) STEM image of a representative $C_3R_6C_3$ trilayer. STEM results indicate that our sample shows good epitaxial growth and atomically sharp interfaces. Annular bright field (ABF) STEM measurements were performed to illustrate the oxygen coordination of SCO in the trilayers. The SCO forms an infinite-layer structure in both trilayers. In $C_3R_6C_3$, C-SCO exhibits vertical-aligned "chain-like" CuO_2 planes with charge neutral SrO^0 and CuO^0 sublayers. As shown in Figure 1c, an oxygen atom moves from CuO_2 layer to the apical oxygen vacancy to maintain charge neutrality. As increasing SCO layer thickness, CuO_2 layers in $C_{12}R_6C_{12}$ transit into a planar-arranged oxygen coordination with Sr^{2+} and CuO_2^{2-} sublayers, resulting in P-SCO has a perovskite-like structure with apical oxygen vacancies (Figure 1e). We also conducted ABF imaging across the SCO-SRO interfaces (Figure S3). Although the stacking sequences of sublayers are different for P-SCO and C-SCO, both interfaces are atomically sharp without significant chemical intermixing due to the polar discontinuity.

https://doi.org/10.1021/acs.nanolett.1c00352
Nano Lett. XXXX, XXX, XXX−XXX

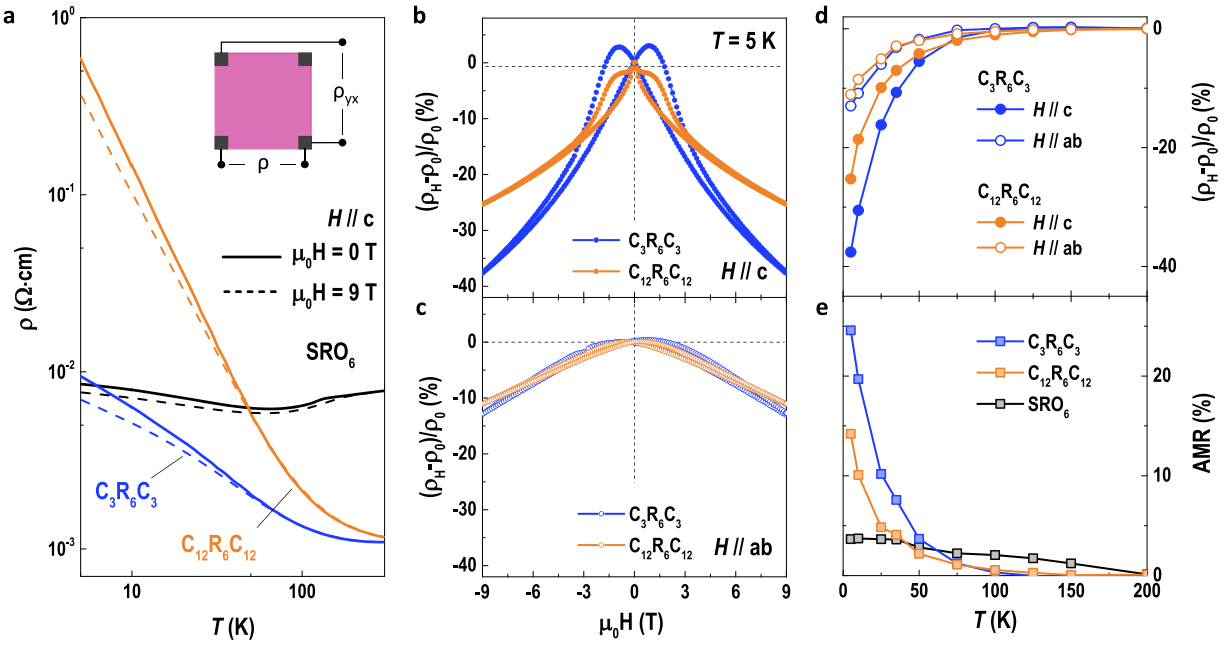

Figure 2. Magnetotransport properties of $C_nR_6C_n$ trilayers. (a) Temperature-dependent resistivity (ρ) of a 6 u.c.-thick SRO single layer (SRO_6), $C_3R_6C_3$, and $C_{12}R_6C_{12}$ trilayers. Solid and dashed lines represent the $\rho-T$ curves measured at 0 and 9 T, respectively. Inset shows the geometry of electrical measurements. Magnetic field dependent magnetoresistances [MR = $(\rho_H-\rho_0)/\rho_0$] were measured at 5 K for $C_3R_6C_3$ and $C_{12}R_6C_{12}$ trilayers. (b, c) MR recorded with magnetic field applied parallel to [001] ($H//c$) and [100] ($H//ab$), respectively. (d) Temperature-dependent MR (top) and anisotropic magnetoresistance (bottom) (AMR = MR_c-MR_{ab}) of SRO_6, $C_3R_6C_3$ and $C_{12}R_6C_{12}$ trilayers.

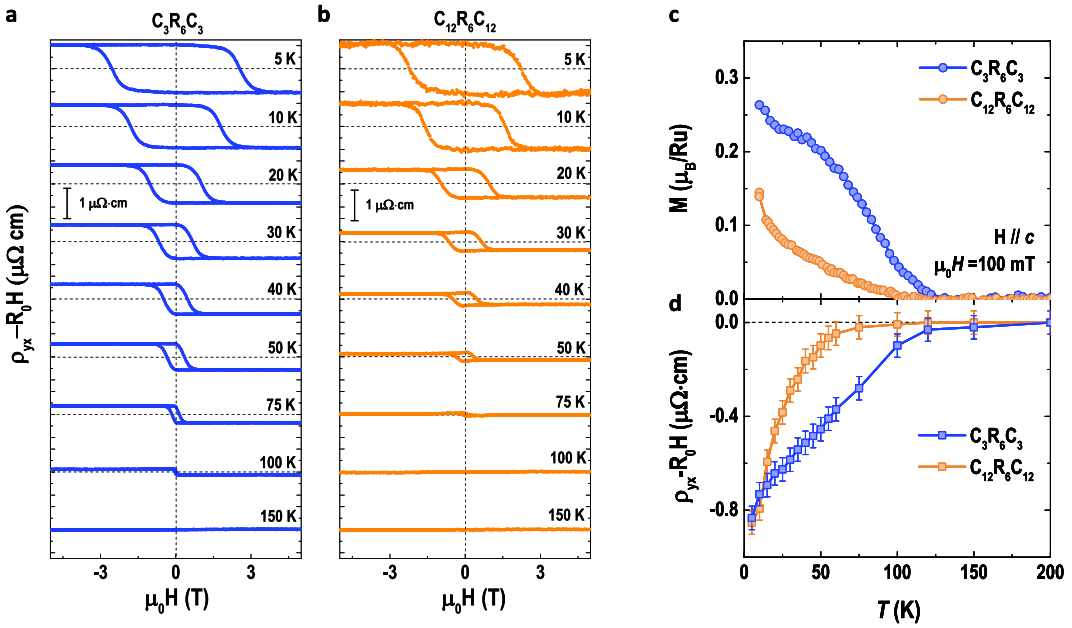

Figure 3. Anomalous Hall resistance of $C_nR_6C_n$ trilayers. (a) Magnetic field-dependent Hall resistance ($\rho_{yx}-R_0H$) of $C_3R_6C_3$ and $C_{12}R_6C_{12}$ trilayers at various temperatures. R_0H represents the ordinary Hall term that is subtracted from ρ_{yx} by linear fitting in the high magnetic field region. ($\rho_{yx}-R_0H$) at each temperature is shifted for clarification. The scale bar of 1 $\mu\Omega$ cm is included. (c) Temperature-dependent M of $C_3R_6C_3$ and $C_{12}R_6C_{12}$ trilayers. M were recorded after field cooling in 100 mT applied along the out-of-plane ($H//c$) direction. (d) Temperature-dependent ($\rho_{yx}-R_0H$) of $C_3R_6C_3$ and $C_{12}R_6C_{12}$ trilayers at μ_0H = 5 T.

The structural transformation in SCO triggers the redistribution of electrons and directly increases the electronic anisotropy. We perform X-ray absorption spectra (XAS) measurements for both O K- and Cu L-edges (Figure S4). The peak intensity in $C_{12}R_6C_{12}$ is larger compared to that of $C_3R_6C_3$, indicating more unoccupied states, i.e. lower electron population, of the hybridized orbitals in $C_{12}R_6C_{12}$. XAS at Cu L-edges for both trilayers confirms the Cu ion keeps a +2-valence state and does not change with oxygen coordination of SCO. Furthermore, X-ray photoelectron spectroscopy (XPS) results on both Cu 2p and Ru 3$p_{3/2}$ confirm that Ru keeps +4-valence, suggesting negligible charge transfer at interfaces (Figure S5). We measured the XAS using the linearly polarized X-ray beam with two different incidence angles (30° and 90°)

https://doi.org/10.1021/acs.nanolett.1c00352
Nano Lett. XXXX, XXX, XXX−XXX

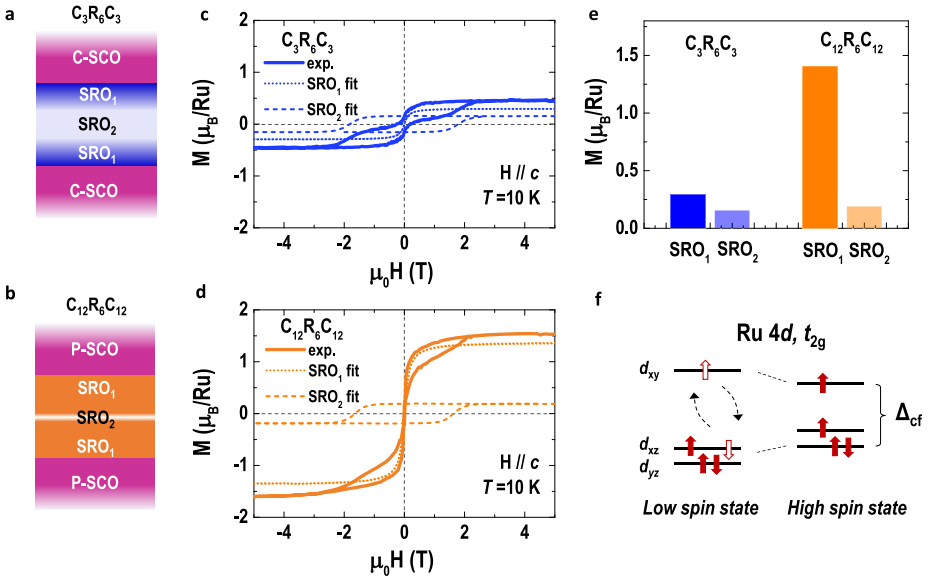

Figure 4. Magnetic properties of $C_nR_6C_n$ trilayers. (a, b) Sample geometries of $C_3R_6C_3$ and $C_{12}R_6C_{12}$ trilayers, respectively. The SRO layers were devided into two parts, SRO_1 and SRO_2. C-SCO and P-SCO represent the chain-type SCO and planar-type SCO, respectively. (c) and (d) Field dependent M measured at 10 K for $C_3R_6C_3$ and $C_{12}R_6C_{12}$ trilayers, respectively. The $M-H$ curves can be fitted by two hysteresis loops contributed from SRO_1 and SRO_2, respectively. The $M-H$ curves from SRO_2 are normalized to the field-dependent anomalous Hall resistivity curves shown in Figure 3. (e) Summary of M_S contributed from SRO_1 and SRO_2 in $C_3R_6C_3$ and $C_{12}R_6C_{12}$ trilayers. The interfacial SRO_1 in two trilayers exhibits a large difference in M_S, whereas the film bulk SRO_2 shows almost identical M_S. (f) Electronic structure of Ru t_{2g} orbital states with low and high spin states. Red solid (empty) arrows represent fully (partially) occupied spin states, which is controlled by the crystal-field energy (Δ_{cf}), i.e., the octahedral tilt angle.

with respect to the surface's plane. We calculate I_c and I_{ab} (Figures 1d, f) which directly reflect the unoccupied states in the out-of-plane and in-plane orbitals, respectively. Direct comparison of orbital polarization in both trilayers, shown in the bottom panels of Figures 1 conducted by calculating the X-ray linear dichroism (XLD = I_c-I_{ab}) of $C_3R_6C_3$ and $C_{12}R_6C_{12}$ trilayers. XLD for $C_3R_6C_3$ is close to zero, suggesting the orbital occupancies of Cu $d_{x^2-y^2}$ and $d_{3z^2-r^2}$ orbitals are nearly equal. In contrast, we observe a nonzero XLD for $C_{12}R_6C_{12}$. At Cu L-edges, I_c is significantly larger than I_{ab}, demonstrating an anisotropic orbital polarization with electrons preferentially occupying the in-plane orbitals.

To evaluate how the bonding geometry of SCO influence the physical properties of adjacent SRO layer, we performed the magnetotransport measurements on both $C_3R_6C_3$ and $C_{12}R_6C_{12}$ trilayers. Figure 2a shows the $\rho-T$ curves when the magnetic fields of 0 and 9 T are applied along the out-of-plane direction. In contrast to the MIT observed in a 6-u.c.-thick SRO single layer, both trilayers exhibit insulating behavior at all temperatures. At 5 K, ρ of $C_{12}R_6C_{12}$ is two orders of magnitude larger than that of $C_3R_6C_3$. We investigate the magnetic anisotropy by measuring the field-dependent magnetoresistances [MR, $(\rho_H-\rho_0)/\rho_0$]. Figures 2b and 2c show MR for both trilayers when $H//c$ and $H//ab$. When $H//c$, the MR of the trilayers shows negative values and symmetric peaks at small H that is coupled with the coercive fields (H_C), in agreement with the typical behavior of a ferromagnet. However, MR reduces dramatically, and the butterfly like hysteresis loops disappear when $H//ab$ (Figures S6 and S7). Figure 2d summarizes MR of $C_3R_6C_3$ and $C_{12}R_6C_{12}$ as a function of temperature. We compare the anisotropic magnetoresistance (AMR, MR_c-MR_{ab}) of two trilayers, as shown in Figure 2e. Comparing to AMR of a SRO single layer, both trilayers show an enormous AMR. Besides, $C_3R_6C_3$ exhibits almost two times larger AMR than that of $C_{12}R_6C_{12}$ (P-SCO), indicating an enhanced magnetic anisotropy induced by C-SCO.

Intriguing magnetic properties of $C_3R_6C_3$ and $C_{12}R_6C_{12}$ trilayers were further investigated by Hall measurements presented in Figure 3. Typically, the Hall resistivity (ρ_{yx}) in a ferromagnet can be expressed as,[20−23] $\rho_{yx} = R_0H + R_SM_z$, where R_0 is the ordinary Hall effect (OHE) coefficient, R_S is the anomalous Hall effect (AHE) coefficient, and M_z is the out-of-plane magnetization. In order to separate the anomalous Hall resistivity from the Hall resistance, the contribution from OHE is subtracted from ρ_{yx}. Therefore, $(\rho_{yx}-R_0H)$ directly represents the spin−orbit coupling and the magnetization of an SRO layer. Because of the temperature dependence of band crossings near the Fermi energy and Berry phase in the momentum space, both temperature and magnetization contribute to anomalous Hall resistivity. Figure 3a,b show the field-dependent $(\rho_{yx}-R_0H)$ at various temperatures for $C_3R_6C_3$ and $C_{12}R_6C_{12}$, respectively. At a fixed temperature, a saturation $(\rho_{yx}-R_0H)$ appears above a critical magnetic field, opening a square-like hysteresis loop. The saturation $(\rho_{yx}-R_0H)$ increases with decreasing temperature. Figure 3d shows the temperature-dependent saturation $(\rho_{yx}\text{-}R_0H)_{5T}$ for both trilayers. A direct comparison of $M-T$ curves for magnetic fields applied along the out-of-plane direction is plotted in Figure 3c. Strikingly, although the $(\rho_{yx}\text{-}R_0H)_{5T}$ is the same for both trilayers at 5 K, $(\rho_{yx}\text{-}R_0H)_{5T}$ in $C_{12}R_6C_{12}$ decays faster than that in $C_3R_6C_3$ with increasing temperature. The AHE curves nearly mimic the $M-T$ trends, demonstrating the magnetic origin of AHE. Please note that the $(\rho_{yx}\text{-}R_0H)-T$ curves do not exhibit hump-like features near H_C, indicating that our SRO layers show neither an intrinsic topological Hall effect[21,24] nor two-channel anomalous Hall effect with opposite sign arising from inhomogeneity.[33,34]

https://doi.org/10.1021/acs.nanolett.1c00352
Nano Lett. XXXX, XXX, XXX−XXX

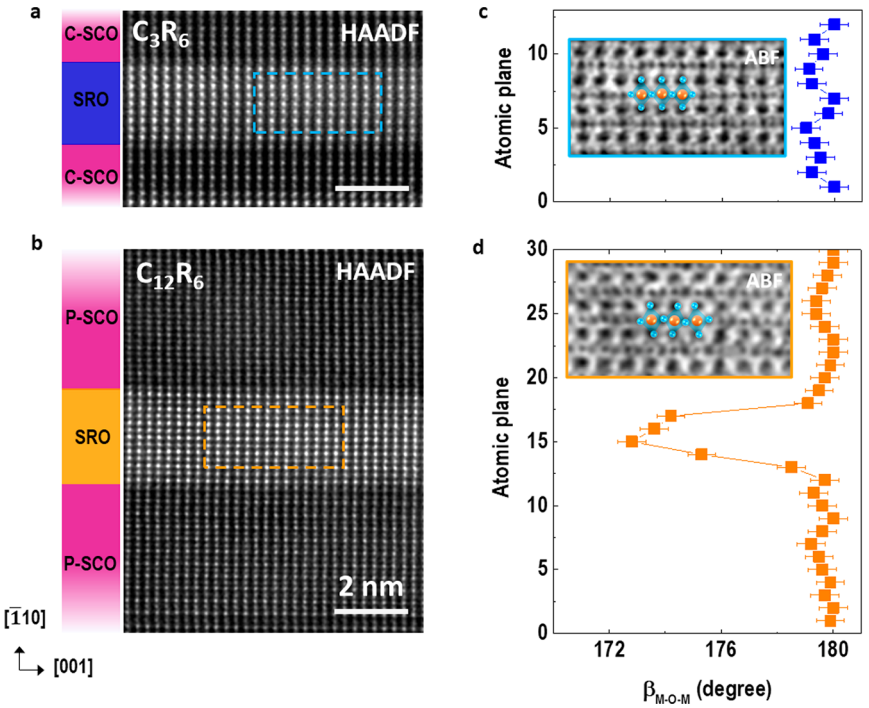

Figure 5. Microstructure characterizations of SRO ultrathin layers sandwiched between two SCO layers. HAADF-STEM images of representative SRO layers sandwiched between (a) 3 u.c. SCO layers and (b) 12 u.c. SCO layers. Samples were imaged along the pseudocubic [110] zone axis in the cross-sectional view. The representative ABF-STEM images from the selected colored dashed regions are shown in the insets of c and d, respectively. The orange and blue spheres in the ABF-STEM images represent the Ru and O atoms, respectively. (c, d) Layer-position-dependent bonding angles ($\beta_{M\text{-}O\text{-}M}$) across the interfaces in C_3R_6 and $C_{12}R_6$ samples, respectively, where M represents transition metal ions (Ru and Cu). The error bars represent one standard deviation.

We further measured the field-dependent magnetization ($M-H$) curves for both trilayers. Both trilayers exhibit a perpendicular magnetic anisotropy (Figure S8). They reach a saturation state with perpendicular field of ~2 T, whereas they are not a fully saturated up to 5 T. Figures 4c and 4d show that the total saturation magnetization (M_S) of $C_{12}R_6C_{12}$ is three times larger than M_S of $C_3R_6C_3$. $M-H$ curves can be well fitted by two hysteresis loops. The dashed and dotted lines in Figures 4c, d represent the different fractions of soft (SRO_1) and hard (SRO_2) magnetic phases in SRO layers, respectively. Therefore, we could logically divide an SRO layer into three parts—two interfacial regions (SRO_1) and one film bulk region (SRO_2), as shown in Figure 4a, b. There is a significant difference in M_S of the soft magnetic hysteresis loops from SRO_1, whereas the SRO_2 in both trilayers shows similar H_C and M_S. Figure 4e summaries the fitted M_S of different magnetic phases in $C_3R_6C_3$ and $C_{12}R_6C_{12}$. The magnetic contribution from SRO_1 enhances from (60 ± 2)% in $C_3R_6C_3$ to (88 ± 2)% in $C_{12}R_6C_{12}$. We attribute these results to the interfacial structural modification. The SRO_1 is adjacent to the SCO layers and is directly affected by the bonding geometry at the interfaces. M_S of SRO_1 is dramatically suppressed when it connected with C-SCO, whereas the M_S of SRO_1 keeps almost the same value (~1.3 μ_B/Ru) as an SRO single layer when it is adjacent to P-SCO. However, SRO_2 is not sensitive to the interfacial modulation. Please note that $M-H$ loops from SRO_2 have identical H_C and similar line shape to the (ρ_{yx}-R_0H)$-T$ curves in both trilayers. Therefore, we could identify that the SRO_1 with small H_C and large M_S is a ferromagnetic insulator with a high spin state and does not contribute to the AHE signals. In contrast, the SRO_2 with large H_C and small M_S is a ferromagnetic semiconductor with a low spin state. The itinerant electrons in SRO_2 lead to the observed AHE in both trilayers. This argument is supported by the insulating behavior evidenced by transport measurements (Figure 2a). $C_{12}R_6C_{12}$ possesses a smaller portion of semiconducting SRO_2 layer, and thus the resistivity of $C_{12}R_6C_{12}$ is larger than that of $C_3R_6C_3$. Because the thicknesses of SRO_2 layers in both trilayers are smaller than the critical thickness for MIT (~6 u.c.), the electronic state of SRO_2 stays in the insulating phase. In addition, we hypothesize that the interfacial electrostatic field could also contribute to the insulating state of SRO_1. In $C_3R_6C_3$, the net charge across the interfaces keeps zero value. However, the interface between P-SCO and SRO is polar, resulting an intrinsic build-in field across the interfaces. Therefore, the electronic reconstruction or charge neutralization may happen within SRO layers. This scenario well explains that the thickness of SRO_1 in $C_{12}R_6C_{12}$ is thicker than that of $C_3R_6C_3$. Furthermore, we performed the polarized neutron reflectivity (PNR) measurements to identify the magnetization distribution across the SRO/SCO interfaces (Figures S9 and S10).[35−39] A $[C_{12}R_6]_{15}$ (15 is bilayer's repeats) superlattice with identical thickness of individual layers was used to increase the total net magnetic moment and the reliability of data fitting with 15 bilayer's repeats. PNR results indicate the SRO layers exhibit a small in-plane magnetization ~0.08 ± 0.02 μ_B/Ru under a magnetic field of 1 T and no magnetization is observed in SCO layers.

To illustrate the microscopic origin of large differences in the magnetization and AHE, we acquire the STEM-ABF images along [110] zone axis to observe oxygen columns and identify the octahedral distortion. Figure 5a, b shows the atomic-resolution HAADF images of SRO ultrathin layers sandwiched by 3 u.c.- and 12 u.c.-thick SCO layers,

https://doi.org/10.1021/acs.nanolett.1c00352
Nano Lett. XXXX, XXX, XXX−XXX

respectively. The representative ABF images from the selected areas marked in (a) and (b) are shown in the insets of Figures 5c, d, respectively. The atomic positions of Ru and O atoms are clearly visible in dark contrast with sub-Å precision. For SRO sandwiched between C-SCO layers, the octahedral tilt is highly suppressed, and the Ru−O−Ru bonding angle is nearly 180° (Figure 5c). Conversely, as indicated in Figure 5d, the Ru−O−Ru bonding angles in $C_{12}R_6C_{12}$ reduces to 173° ± 0.3°. The sharp discrepancy in octahedral distortion between two cases can be attributed to the strong modulation of structural parameters. Although all layers are coherently strained to STO substrates, e. g. subject to the same misfit strain, the out-of-plane lattice constants of SRO are ∼3.96 ± 0.03 Å and ∼3.90 ± 0.02 Å in $C_3R_6C_3$ and $C_{12}R_6C_{12}$, respectively. The reduction of the out-of-plane lattice constants propagates from the adjacent SCO layers into the SRO layers. In $C_3R_6C_3$ with C-SCO, SRO could keep its RuO_6 octahedra without structural deformation. However, SRO would undergo a significant structural distortion to overcome the apical oxygen vacancies in the P-SCO, hindering its elastic deformation under the substrate-induced epitaxial strain. We calculate the tetragonality c/a is 1.014 ± 0.007 and 0.998 ± 0.005 for SRO in $C_3R_6C_3$ and $C_{12}R_6C_{12}$, respectively. Under the same misfit strain, SRO in $C_3R_6C_3$ is more tetragonally distorted than SRO in $C_{12}R_6C_{12}$. Earlier work on the He-implanted single film had demonstrated that a bulk-like orthorhombically distorted phase can be shift to a tetragonal structure by elongating uniaxially along the out-of-plane direction.[40] The dramatic phase transition is accompanied by an octahedral rotation pattern change from $a^-a^+c^-$ into $a^0a^0c^-$ when c/a increases. Similarly, SRO single films grown on different substrates suffer the lattice-mismatch strain. The octahedral tilt preferentially occurs in the tensile-strained SRO ($c/a < 1$) layers.[41] These results are consistent with our experimental observations.

The microstructural distortion provides a solid evidence in the observed magnetization contrast in the SRO layers adjacent to different-type of SCO layers. In SRO with tilted octahedra, four electrons occupy the t_{2g} orbitals with lowest energy cost, exhibiting a high spin state (Figure 4f). The crystal field splitting energy Δ_{cf} is known to be proportional to $1/d^5$, where d is the Ru−O bond length. Because epitaxial grown SRO is compressively strained, a flattened Ru−O−Ru bond in $C_3R_6C_3$ leads to a smaller bond length, thus Δ_{cf} in $C_3R_6C_3$ is larger than that of $C_{12}R_6C_{12}$. Therefore, a larger splitting between d_{xy} and d_{xz} orbitals appears, resulting in one itinerant electron between two nearby orbitals. According to the Hund's Rules, the electron would flip its sign when it stays in the d_{xz} orbital. The change of electronic states leads to a reduced saturation magnetization of SRO. The proposed scenario agrees with our experimental results that the magnetization of $C_3R_6C_3$ is smaller than that of $C_{12}R_6C_{12}$. Our results consistently agree with a previous theoretical prediction by Herklotz et al.[42] and a recent experimental work by Jeong et al.[26] These results consistently support the spin state of Ru is effectively controlled by crystallographic parameters which are connected to the adjacent oxygen coordination.

In summary, we report the structural modification of SRO layers in proximity to SCO with infinite-layer structure. The octahedral tilt in the SRO is strongly associated with oxygen coordination of SCO. When the CuO_2 infinite layers have a "chain-type" structure, the adjacent SRO exhibits a large magnetic anisotropy and anomalous Hall resistance. The opposite results are observed in the SRO layer connecting to the SCO has "planar-type" CuO_2 infinite layers. The selective manipulation of octahedral distortion in functional oxides provides an effective means to engineer the local structural parameters which link their transport and magnetic properties. Especially, our results establish a methodology of propagation the out-of-plane lattice constants from the structural dissimilar materials into the functional oxides with a fixed in-plane misfit strain. This approach adds another tuning knob to fine-control the interplay between competing electronic and magnetic order parameters in the artificial oxide heterostructures.

METHODS

Sample Synthesis and Basic Characterizations. Trilayers and superlattices consisting of SRO and SCO were prepared on (001)-oriented STO substrates by PLD. The thickness of SRO layer is fixed to 6 u.c. and the SCO layers are 3 and 12 u.c. thick in the trilayers and superlattices. The magnetic and transport properties were measured using PPMS and SQUID. Standard van der Pauw method was used in the resistivity and Hall measurements. The $[C_nR_6]_{15}$ superlattices were used for PNR and STEM characterizations.

STEM Characterizations. The samples were prepared using ion milling after the mechanical thinning and were examined by STEM. The trilayer samples were measured along the pseudocubic [100] zone axis using a Titan Themis double-corrected TEM at Wuhan University of Technology. The $[C_nR_6]_{15}$ superlattices were investigated along the pseudocubic [110] zone axis using a JEM ARM200CF microscopy at Institute of Physics of Chinese Academy of Sciences.

X-ray Spectroscopic Measurements. Room-temperature XAS measurements were conducted in the total electron yield mode for both Cu L- and O K-edges at beamline 4B9B of the Beijing Synchrotron Radiation Facility. The sample's scattering plane was rotated at the angle of 30 and 90° with respect to the direction of incident X-ray beam. When the X-ray beam was perpendicular to the samples' surface, the in-plane orbital information was obtained ($I_{ab} = I_{90°}$). The out-of-plane orbital information can be calculated by $I_c = (I_{90°} - I_{30°}\cdot\sin^2 30°)/\cos^2 30°$.

PNR Measurements. PNR measurements on the $[C_{12}R_6]_{15}$ superlattice were performed on both Beamline 4A at Spallation Neutron Source of Oak Ridge National Laboratory and Multipurpose Reflectometer beamline at the Chinese Spallation Neutron Source. The sample was cooled down to 10 K under an in-plane magnetic field of 1 T. The spin-polarization dependent specular reflectivity was measured as a function of the wave vector transfer along the film surface normal. R^+ and R^- are the reflectivities from the spin-up and spin-down polarized neutrons, respectively.

ASSOCIATED CONTENT

Supporting Information

The Supporting Information is available free of charge at https://pubs.acs.org/doi/10.1021/acs.nanolett.1c00352.

Details on the physical property characterizations of SRO single layers, $C_3R_6C_3$, and $C_{12}R_6C_{12}$ trilayers; interface microstructures; electronic state characterizations; in-plane and out-of-plane magneto transport measurements; magnetic hysteresis loops, and PNR results (PDF)

https://doi.org/10.1021/acs.nanolett.1c00352
Nano Lett. XXXX, XXX, XXX−XXX

AUTHOR INFORMATION

Corresponding Authors

Kuijuan Jin − *Beijing National Laboratory for Condensed Matter Physics and Institute of Physics, Chinese Academy of Sciences, Beijing 100190, China; School of Physical Sciences, University of Chinese Academy of Sciences, Beijing 100190, China; Songshan Lake Materials Laboratory, Dongguan, Guangdong 523808, China;* orcid.org/0000-0002-0047-4375; Email: kjjin@iphy.ac.cn

Er-Jia Guo − *Beijing National Laboratory for Condensed Matter Physics and Institute of Physics, Chinese Academy of Sciences, Beijing 100190, China; Center of Materials Science and Optoelectronics Engineering, University of Chinese Academy of Sciences, Beijing 100049, China; School of Physical Sciences, University of Chinese Academy of Sciences, Beijing 100190, China; Songshan Lake Materials Laboratory, Dongguan, Guangdong 523808, China;* orcid.org/0000-0001-5702-225X; Email: ejguo@iphy.ac.cn

Authors

Shan Lin − *Beijing National Laboratory for Condensed Matter Physics and Institute of Physics, Chinese Academy of Sciences, Beijing 100190, China; Center of Materials Science and Optoelectronics Engineering, University of Chinese Academy of Sciences, Beijing 100049, China*

Qinghua Zhang − *Beijing National Laboratory for Condensed Matter Physics and Institute of Physics, Chinese Academy of Sciences, Beijing 100190, China*

Xiahan Sang − *State Key Laboratory of Advanced Technology for Materials Synthesis and Processing and Nanostructure Research Center, Wuhan University of Technology, Wuhan 430070, China;* orcid.org/0000-0002-2861-6814

Jiali Zhao − *Beijing National Laboratory for Condensed Matter Physics and Institute of Physics, Chinese Academy of Sciences, Beijing 100190, China*

Sheng Cheng − *Spallation Neutron Source Science Center, Dongguan 523803, China*

Amanda Huon − *Neutron Scattering Division and Materials Science and Technology Division, Oak Ridge National Laboratory, Oak Ridge, Tennessee 37831, United States*

Qiao Jin − *Beijing National Laboratory for Condensed Matter Physics and Institute of Physics, Chinese Academy of Sciences, Beijing 100190, China; School of Physical Sciences, University of Chinese Academy of Sciences, Beijing 100190, China*

Shuang Chen − *Beijing National Laboratory for Condensed Matter Physics and Institute of Physics, Chinese Academy of Sciences, Beijing 100190, China; School of Physical Engineering, Zhengzhou University, Zhengzhou 450001, China*

Shengru Chen − *Beijing National Laboratory for Condensed Matter Physics and Institute of Physics, Chinese Academy of Sciences, Beijing 100190, China; School of Physical Sciences, University of Chinese Academy of Sciences, Beijing 100190, China*

Wenjun Cui − *State Key Laboratory of Advanced Technology for Materials Synthesis and Processing and Nanostructure Research Center, Wuhan University of Technology, Wuhan 430070, China*

Haizhong Guo − *School of Physics and Microelectronics, Zhengzhou University, Zhengzhou 450001, China;* orcid.org/0000-0002-6128-4225

Meng He − *Beijing National Laboratory for Condensed Matter Physics and Institute of Physics, Chinese Academy of Sciences, Beijing 100190, China*

Chen Ge − *Beijing National Laboratory for Condensed Matter Physics and Institute of Physics, Chinese Academy of Sciences, Beijing 100190, China;* orcid.org/0000-0002-8093-940X

Can Wang − *Beijing National Laboratory for Condensed Matter Physics and Institute of Physics, Chinese Academy of Sciences, Beijing 100190, China; School of Physical Sciences, University of Chinese Academy of Sciences, Beijing 100190, China; Songshan Lake Materials Laboratory, Dongguan, Guangdong 523808, China;* orcid.org/0000-0002-4404-7957

Jiaou Wang − *Institute of High Energy Physics, Chinese Academy of Sciences, Beijing 100049, China*

Michael R. Fitzsimmons − *Neutron Scattering Division, Oak Ridge National Laboratory, Oak Ridge, Tennessee 37831, United States; Department of Physics and Astronomy, University of Tennessee, Knoxville, Tennessee 37996, United States*

Lin Gu − *Beijing National Laboratory for Condensed Matter Physics and Institute of Physics, Chinese Academy of Sciences, Beijing 100190, China; School of Physical Sciences, University of Chinese Academy of Sciences, Beijing 100190, China; Songshan Lake Materials Laboratory, Dongguan, Guangdong 523808, China;* orcid.org/0000-0002-7504-031X

Tao Zhu − *Beijing National Laboratory for Condensed Matter Physics and Institute of Physics, Chinese Academy of Sciences, Beijing 100190, China; School of Physical Sciences, University of Chinese Academy of Sciences, Beijing 100190, China; Spallation Neutron Source Science Center, Dongguan 523803, China; Songshan Lake Materials Laboratory, Dongguan, Guangdong 523808, China*

Complete contact information is available at: https://pubs.acs.org/10.1021/acs.nanolett.1c00352

Author Contributions

E.J.G. initiated the research and supervised the project. These samples were grown by S. L.; TEM lamellas were fabricated with FIB milling and TEM experiments were performed by Q.H.Z., X.H.S., and L.G.; XAS measurements were conducted by S.L., J Z., Q.J., S.C., S.C., and J.O.W.; Magnetic measurements were performed by S.L., H.G.; PNR measurements were performed by A.H., M.R.F., and T.Z.; S.L. and E.J.G. wrote the manuscript with help from K.J.J. All authors participated in discussion of the manuscript.

Notes

The authors declare no competing financial interest.

ACKNOWLEDGMENTS

The authors greatly appreciate the fruitful discussions with Prof. Hanghui Chen at NYU Shanghai. This work was supported by the National Key Basic Research Program of China (Grants 2019YFA0308500 and 2020YFA0309100), the National Natural Science Foundation of China (Grants 11974390, 51902237, 52025025, and 52072400), the Beijing Nova Program of Science and Technology (Grant Z191100001119112), the Beijing Natural Science Foundation (Grant 2202060), the program for the Innovation Team of Science and Technology in University of Henan

https://doi.org/10.1021/acs.nanolett.1c00352
Nano Lett. XXXX, XXX, XXX−XXX

(20IRTSTHN014), and the Strategic Priority Research Program (B) of the Chinese Academy of Sciences (Grant XDB33030200). The XAS and XLD experiments at the beamline 4B9B of the Beijing Synchrotron Radiation Facility (BSRF) of the Institute of High Energy Physics, Chinese Academy of Sciences, were conducted via a user proposal. PNR measurements at the Chinese Spallation Neutron Source (CSNS) were conducted via a user proposal (P2018121100016). The research at ORNL's SNS (PNR measurements), which is a U.S. Department of Energy (DOE), Office of Science (OS), Basic Energy Sciences (BES) scientific user facility, was conducted via a user proposal.

REFERENCES

(1) Rondinelli, J. M.; et al. Control of octahedral connectivity in perovskite oxide heterostructures: An emerging route to multifunctional materials discovery. *MRS Bull.* **2012**, *37*, 261−270.
(2) Moon, E. J.; et al. Spatial control of functional properties via octahedral modulations in complex oxide superlattices. *Nat. Commun.* **2014**, *5*, 5710.
(3) Imada, M.; Fujimori, A.; Tokura, Y. Metal-insulator transitions. *Rev. Mod. Phys.* **1998**, *70*, 1039.
(4) Zubko, P.; Gariglio, S.; Gabay, M.; Ghosez, P.; Triscone, J.-M. Interface Physics in Complex Oxide Heterostructures. *Annu. Rev. Condens. Matter Phys.* **2011**, *2*, 141−165.
(5) Schlom, D. G.; et al. Strain Tuning of Ferroelectric Thin Films. *Annu. Rev. Mater. Res.* **2007**, *37*, 589−626.
(6) Locquet, J. P.; et al. Doubling the critical temperature of $La_{1.9}Sr_{0.1}CuO_4$ using epitaxial strain. *Nature* **1998**, *394*, 453.
(7) Lee, H. N.; et al. Strong polarization enhancement in asymmetric three-component ferroelectric superlattices. *Nature* **2005**, *433*, 395.
(8) Haeni, J. H.; et al. Room-temperature ferroelectricity in strained $SrTiO_3$. *Nature* **2004**, *430*, 758.
(9) Boris, A. V.; et al. Dimensionality Control of Electronic Phase Transitions in Nickel-Oxide Superlattices. *Science* **2011**, *332*, 937.
(10) Gan, Q.; Rao, R. A.; Eom, C. B.; Garrett, J. L.; Lee, M. Direct measurement of strain effects on magnetic and electrical properties of epitaxial $SrRuO_3$ thin films. *Appl. Phys. Lett.* **1998**, *72*, 978.
(11) Koster, G.; Klein, L.; Siemons, W.; Rijnders, G.; Dodge, J. S.; Eom, C. B.; Blank, D. H. A.; Beasley, M. R. Structure, physical properties, and applications of $SrRuO_3$ thin films. *Rev. Mod. Phys.* **2012**, *84*, 253.
(12) Kan, D.; Shimakawa, Y.; et al. Strain Effect on Structural Transition in $SrRuO_3$ Epitaxial Thin Films. *Cryst. Growth Des.* **2011**, *11*, 5483−5487.
(13) Xia, J.; Siemons, W.; Koster, G.; Beasley, M. R.; Kapitulnik, A. Critical thickness for itinerant ferromagnetism in ultrathin films of $SrRuO_3$. *Phys. Rev. B: Condens. Matter Mater. Phys.* **2009**, *79*, 140407.
(14) Aso, R.; et al. Strong Dependence of Oxygen Octahedral Distortions in $SrRuO_3$ Films on Types of Substrate-Induced Epitaxial Strain. *Cryst. Growth Des.* **2014**, *14*, 6478−6485.
(15) Kats, Y.; Genish, I.; Klein, L.; Reiner, J. W.; Beasley, M. R. Large anisotropy in the paramagnetic susceptibility of $SrRuO_3$ films. *Phys. Rev. B: Condens. Matter Mater. Phys.* **2005**, *71*, 100403.
(16) Toyota, D.; Ohkubo, I.; Kumigashira, H.; Oshima, M.; Ohnishi, T.; Lippmaa, M.; Takizawa, M.; Fujimori, A.; Ono, K.; Kawasaki, M.; Koinuma, H. Thickness-dependent electronic structure of ultrathin SrRuO3 films studied by in situ photoemission spectroscopy. *Appl. Phys. Lett.* **2005**, *87*, 162508.
(17) Kan, D.; et al. Tuning magnetic anisotropy by interfacially engineering the oxygen coordination environment in a transition metal oxide. *Nat. Mater.* **2016**, *15*, 432.
(18) Thomas, S.; et al. Localized Control of Curie Temperature in Perovskite Oxide Film by Capping-Layer-Induced Octahedral Distortion. *Phys. Rev. Lett.* **2017**, *119*, 177203.
(19) Lin, S.; et al. Switching Magnetic Anisotropy of $SrRuO_3$ by Capping-Layer-Induced Octahedral Distortion. *Phys. Rev. Appl.* **2020**, *13*, 034033.
(20) Fang, Z.; Nagaosa, N.; Takahashi, K. S.; Asamitsu, A.; Mathieu, R.; Ogasawara, T.; Yamada, H.; Kawasaki, M.; Tokura, Y.; Terakura, K. Anomalous Hall Effect and Magnetic Monopoles in Momentum-Space. *Science* **2003**, *302*, 92.
(21) Matsuno, J.; Ogawa, N.; Yasuda, K.; Kagawa, F.; Koshibae, W.; Nagaosa, N.; Tokura, Y.; Kawasaki, M. Interface-driven topological Hall effect in $SrRuO_3$-$SrIrO_3$ bilayer. *Sci. Adv.* **2016**, *2*, No. e1600304.
(22) Qin, Q.; et al. Emergence of Topological Hall Effect in a $SrRuO_3$ Single Layer. *Adv. Mater.* **2019**, *31*, 1807008.
(23) Gu, Y.; Wei, Y.-W.; Xu, K.; Zhang, H.; Wang, F.; Li, F.; Saleem, M. S.; Chang, C.-Z.; Sun, J.; Song, C.; Feng, J.; Zhong, X.; Liu, W.; Zhang, Z.; Zhu, J.; Pan, F. Interfacial oxygen-octahedral-tilting-driven electrically tunable topological Hall effect in ultrathin $SrRuO_3$ films. *J. Phys. D: Appl. Phys.* **2019**, *52*, 404001.
(24) Wang, L.; Feng, Q.; Kim, Y.; Kim, R.; Lee, K. H.; Pollard, S. D.; Shin, Y. J.; Zhou, H.; Peng, W.; Lee, D.; Meng, W.; Yang, H.; Han, J. H.; Kim, M.; Lu, Q.; Noh, T. W. Ferroelectrically tunable magnetic skyrmions in ultrathin oxide heterostructures. *Nat. Mater.* **2018**, *17*, 1087−1094.
(25) Cui, Z.; Grutter, A. J.; Zhou, H.; Cao, H.; Dong, Y.; Gilbert, D. A.; Wang, J.; Liu, Y. S.; Ma, J.; Hu, Z.; Guo, J.; Xia, J.; Kirby, B. J.; Shafer, P.; Arenholz, E.; Chen, H.; Zhai, X.; Lu, Y. Correlation-driven eightfold magnetic anisotropy in a two-dimensional oxide monolayer. *Sci. Adv.* **2020**, *6*, No. eaay0114.
(26) Jeong, S. G.; et al. Propagation Control of Octahedral Tilt in $SrRuO_3$ via Artificial Heterostructuring. *Adv. Sci.* **2020**, *7*, 2001643.
(27) Boschker, H.; et al. Ferromagnetism and Conductivity in Atomically Thin $SrRuO_3$. *Phys. Rev. X* **2019**, *9*, 011027.
(28) Jeong, S. G.; Min, T.; Woo, S.; Kim, J.; Zhang, Y.-Q.; Cho, S. W.; Son, J.; Kim, Y.-M.; Han, J. H.; Park, S.; et al. Phase Instability amid Dimensional Crossover in Artificial Oxide Crystal. *Phys. Rev. Lett.* **2020**, *124*, 026401.
(29) Zaliznyak, I. A.; Broholm, C.; Kibune, M.; Nohara, M.; Takagi, H. Anisotropic Spin Freezing in the S = 1/2 Zigzag Chain Compound $SrCuO_2$. *Phys. Rev. Lett.* **1999**, *83*, 5370.
(30) Zhong, Z. C.; Koster, G.; Kelly, P. J. Prediction of thickness limits of ideal polar ultrathin films. *Phys. Rev. B: Condens. Matter Mater. Phys.* **2012**, *85*, 121411.
(31) Samal, D.; Tan, H.; Molegraaf, H.; Kuiper, B.; Siemons, W.; Bals, S.; Verbeeck, J.; Van Tendeloo, G.; Takamura, Y.; Arenholz, E.; et al. Experimental Evidence for Oxygen Sublattice Control in Polar Infinite Layer $SrCuO_2$. *Phys. Rev. Lett.* **2013**, *111*, 096102.
(32) Liao, Z.; Skoropata, E.; Freeland, J. W.; Guo, E. J.; Desautels, R.; Gao, X.; Sohn, C.; Rastogi, A.; Ward, T. Z.; Zou, T.; et al. Large orbital polarization in nickelate-cuprate heterostructures by dimensional control of oxygen coordination. *Nat. Commun.* **2019**, *10*, 589.
(33) Kimbell, G.; Sass, P. M.; Woltjes, B.; Ko, E. K.; Noh, T. W.; Wu, W.; Robinson, J. W. A. Two-channel anomalous Hall effect in $SrRuO_3$. *Phys. Rev. Mater.* **2020**, *4*, 054414.
(34) Wu, L.; Wen, F.; Fu, Y.; Wilson, J. H.; Liu, X.; Zhang, Y.; Vasiukov, D. M.; Kareev, M. S.; Pixley, J. H.; Chakhalian, J. Berry phase manipulation in ultrathin $SrRuO_3$ Films. *Phys. Rev. B* **2020**, *102*, No. 220406(R).
(35) Chakhalian, J.; Freeland, J. W.; Habermeier, H.-U.; Cristiani, G.; Khaliullin, G.; van Veenendaal, M.; Keimer, B. Orbital reconstruction and covalent bonding at an oxide interface. *Science* **2007**, *318*, 1114−1117.
(36) Chakhalian, J.; Freeland, J. W.; Srajer, G.; Strempfer, J.; Khaliullin, G.; Cezar, J. C.; Charlton, T.; Dalgliesh, R.; Bernhard, C.; Cristiani, G.; Habermeier, H.-U.; Keimer, B. Magnetism at the interface between ferromagnetic and superconducting oxides. *Nat. Phys.* **2006**, *2*, 244−248.
(37) Fitzsimmons, M. R.; Bader, S. D.; Borchers, J. A.; Felcher, G. P.; Furdyna, J. K.; Hoffmann, A.; Kortright, J. B.; Schuller, I. K.; Schulthess, T. C.; Sinha, S. K.; Toney, M. F.; Weller, D.; Wolf, S. Neutron scattering studies of nanomagnetism and artificially structured materials. *J. Magn. Magn. Mater.* **2004**, *271*, 103.
(38) Singh, S.; Haraldsen, J. T.; Xiong, J.; Choi, E. M.; Lu, P.; Yi, D.; Wen, X.-D.; Liu, J.; Wang, H.; Bi, Z.; Yu, P.; Fitzsimmons, M. R.;

https://doi.org/10.1021/acs.nanolett.1c00352
Nano Lett. XXXX, XXX, XXX−XXX

MacManus-Driscoll, J. L.; Ramesh, R.; Balatsky, A. V.; Zhu, J. X.; Jia, Q. X. Induced magnetization in $La_{0.7}Sr_{0.3}MnO_3/BiFeO_3$ superlattices. *Phys. Rev. Lett.* **2014**, *113*, 047204.
(39) Guo, E. J.; Petrie, J. R.; Roldan, M. A.; Li, Q.; Desautels, R. D.; Charlton, T.; Herklotz, A.; Nichols, J.; van Lierop, J.; Freeland, J. W.; Kalinin, S. V.; Lee, H. N.; Fitzsimmons, M. R. Spatially Resolved Large Magnetization in Ultrathin $BiFeO_3$. *Adv. Mater.* **2017**, *29*, 1700790.
(40) Herklotz, A.; Wong, A. T.; Meyer, T.; Biegalski, M. D.; Lee, H. N.; Ward, T. Z. Controlling Octahedral Rotations in a Perovskite via Strain Doping. *Sci. Rep.* **2016**, *6*, 26491.
(41) Aso, R.; Kan, D.; Shimakawa, Y.; Kurata, H. Control of Structural Distortions in Transition-Metal Oxide Films through Oxygen Displacement at the Heterointerface. *Adv. Funct. Mater.* **2014**, *24*, 5177−5184.
(42) Herklotz, A.; Doerr, K. Characterization of tetragonal phases of $SrRuO_3$ under epitaxial strain by density functional theory. *Eur. Phys. J. B* **2015**, *88*, 60.

https://doi.org/10.1021/acs.nanolett.1c00352
Nano Lett. XXXX, XXX, XXX−XXX